TURBULENT FLOWFIELD STRUCTURE ASSOCIATED TO FIN BUFFETING AROUND A VORTEX–DOMINATED AIRCRAFT CONFIGURATION AT SIDESLIP

Christian Breitsamter and Boris Laschka
Research Engineer, Full Professor of Fluid Mechanics
Lehrstuhl für Fluidmechanik, Technische Universität München,
D-80290 München,
Germany

Abstract

Selected results from a comprehensive experimental investigation are presented for the low-speed flow environment in the fin region of a delta–canard–configuration. Laser light sheet flow visualization is used to look at the various sources of vortex generation, and the evolution of these vortices. Hot–wire anemometry is applied to quantify detailed flowfields of the time–dependent three–dimensional velocity field from moderate to high angles of attack and at sideslip conditions. Test Reynolds number was 1.0×10^6. Time–averaged, root-mean-square and spectral distributions are evaluated to study the structure of the highly turbulent vortex dominated flowfield. With increasing incidence, in particular, at sideslip the wing and the canard vortex systems are shifted inboard. They increase the velocity fluctuations in the vicinity of the mid section. The power spectra density show significant frequency peaks related to the concentration of kinetic turbulent energy in the flow of the wing/canard vortex sheet. Because of the asymmetric flow at sideslip, at high incidences the vortex sheet associated with a narrow–band turbulent energy is approaching the plane of symmetry. This is an indication that fin oscillations may be excited by narrow–band flow fluctuations, in particular, at vortex burst at high incidence. By comparison with symmetric flow conditions sideslip may cause a substantial increase in the excitation on a single fin and its response.

Nomenclature

Symbols:

f	frequency, Hz
g	constant of gravitation
k	reduced frequency, fl_μ/U_∞
l_i	wing root chord
l_μ	wing mean aerodynamic chord
Re	Reynolds number, $U_\infty l_\mu/\nu$
s	wing half span
U_∞	freestream velocity
u, v, w	streamwise, lateral and vertical velocity components (wind tunnel-axis system)
$\overline{u}, \overline{v}, \overline{w}$	streamwise, lateral and vertical mean velocity
u', v', w'	fluctuation part of u, v, w
u_{rms}, v_{rms}, w_{rms}	root-mean-square values of the fluctuating components of velocity, $u_{rms} = \sqrt{\overline{u'^2}}$, $v_{rms} = \sqrt{\overline{v'^2}}$, $w_{rms} = \sqrt{\overline{w'^2}}$
$u_{xz_{rms}}$	root-mean-square value of the streamwise and vertical fluctuating components
Y, Z	non-dimensionalized coordinates in the measurement plane, referred to s, origin at the mid section
x, y, z	streamwise, lateral and vertical coordinates of the wind tunnel–axis system
α	aircraft angle of attack
φ_W	wing leading–edge sweep
φ_C	canard leading–edge sweep
Λ	wing aspect ratio
λ	wing taper ratio
ν	kinematic viscosity
ω_x	axial vorticity, $1/2\,(\partial\overline{w}/\partial y - \partial\overline{v}/\partial z)$
Ω_x	dimensionless axial vorticity, $\omega s/U_\infty$

Abbreviations:

rms	root-mean-square

Introduction

High–performance fighter aircraft achieve enhanced manouverability at high angles of attack due to vortex-induced lift characteristic and close–coupled canard control devices. Canard–delta wing type plays an important role in the development of air combat supermanouevers which require the maintenance of controlled flight at high angle of attack for extended periods.

Severe fin buffeting has been encounterd on leading–edge vortex–dominated configurations during operation at high angle of attack.[1] At F/A–18 flight tests peak accelerations were measured up to 450 g at a position close to the tip of the port fin.[2] Similar phenomena have been observed on the single–finned X–29 and X–31 research vehicles.[3] From wind tunnel tests performed on such aircraft fin buffeting has been attributed to vortex flow enveloping the fin(s), where narrow–band aerodynamic loads excite at the natural frequencies the fin structure, in particular, when vortex bursting occurs.[1,4–9] Under these conditions vibration free control and long fatigue life have become crucial issues and consequently, the angle–of–attack envelope of the aircraft may be limited.

This situation has initiated a number of studies on fin buffeting of vortex–dominated aircraft configurations.[5,6] Comprehensive tests on twin–fin fighter aircraft (F/A–18, F–15, YF–17) provide data which refer to steady and unsteady forces and moments,[10,11] steady and unsteady field

and surface pressure measurements,[7,9,11–13] and small-scale wind-tunnel fin pressure measurements and vertical tail acceleration data from flight test.[2,14] Fin buffeting becomes severe when the leading-edge vortex bursts ahead of the vertical tail(s). Investigations related to this subject focus also on the vortex structure and the vortex-breakdown phenomenon using water-tunnel experiments [8], laser light sheet flow visualization[15] as well as velocity flowfield surveys[16,17]. After the rapid expansion of the vortex core due to burst the flow changes to a highly turbulent swirling state. It causes large velocity fluctuations with a narrow-band concentration of kinetic turbulent energy.[1,16] Small-scale low-speed wind tunnel tests on the F-15 twin-fin flow environment show also peaked velocity spectra inboard and outboard of the vertical tails at high incidence.[18,19]

Extensive programs aimed at the understanding and reducing the buffeting loads on F-15 and F/A-18 vertical tails are summarized in Ref. 5, 20. Efforts to alleviate buffet loads deal with design modifications e.g. use of streamwise LEX-fences,[2] concepts of active control[5] and, more academically, tangential leading-edge blowing which shifts the buffeting excitation and response to higher angles of attack.[21]

The problem of extrapolating model-scale data to flight tests depends on the flow characteristics due to changes in Reynolds and Mach number. In the context of high-α aerodynamics the comparison of vortex burst locations between water tunnel experiments and actual flight tests of the F/A-18 shows a highly accurate correlation.[22] For the particular case of fighter-type aircraft, characterized by highly swept wings with sharp leading edges, the flow separates at the leading edge regardless of Reynolds number. Also, most manoeuvres at high angle of attack are associated with low Mach numbers due to structural limitations. Experimental data obtained at different Reynolds and Mach numbers may be influenced by surface roughness, tunnel turbulence, wall effects, and model support interference.[15]

Methods for predicting wing response to buffet loads are described in Ref. 23 – 26. It was shown that buffet spectra could be extrapolated over large ranges of velocity, and model size, and that they could be used to predict flight loads. Ref. 26 presents an analytical model to generate a fluctuating flowfield producing unsteady pressures due to vortex breakdown. This method is based on test data of the mean square values of fluctuating normal forces. Thus, there is a strong need for the measurement of the fluctuating velocity components in a buffeting inducing flowfield.

Present Scope and Objectives

A general treatment of the fin buffeting problem requires detailed instantaneous flowfield data to understand the properties of the very complex vortical flow in the fin region associated with the bursting of the leading-edge vortices. As a contribution to fill this gap, a research program on a typical high performance aircraft model was initiated at the Lehrstuhl für Fluidmechanik of the Technische Universität München.

The present investigation focus on the spatial and temporal characteristics of the turbulent flow structure around vortex-dominated aircraft configurations at moderate and at high angle of attack. The approach adopted here is to measure the fluctuating velocity components in the fin region. In Ref. 1 the flow at zero sideslip angle has been investigated. In the present paper that investigation has been extended to sideslip conditions. Statistical analysis is applied to identify dominant flowfield phenomena.

This supports an attempt to formulate a model for fin buffeting aerodynamic loads. They utilize features of the flowfield which are dependent on the aircraft configuration and aerodynamic conditions such as the angle of attack and sideslip. It is highly desirable to be able to assess buffeting loads without resolving detailed unsteady measurements of fin surface pressure. As any model can be used this results in a siginificant reduction of model costs. The multifaceted and detailed flowfield surveys can be used to validate the computational prediction methods. Only limited high-speed wind tunnel data and some flight data are necessary to be used as check points, to predict the fin-buffeting full-scale flight environment.

Experimental Technique and Test Program

Facility and Model Description

All experiments were carried out in one of the low-speed wind tunnels of the Technische Universität München. It is a closed-return facility. The nozzle diameter is 1.5 m, the length of the open test section is 3 m. Maximum usable velocity is 55 m/s. Turbulence intensity is known to be under 0.3% – 0.4% over the speed range of interest. The minimum steps for the three-degree-of-freedom probe-traversing system in the streamwise, spanwise and normal directions are $\pm$0.2 mm.

The tunnel is equipped with an automated data acquisiton and control system. A personal computer with a high-speed board is used for data acquisition of the hot-wire, pressure and temperature signals as well as for the control of the wind tunnel, the 3-axis probe-traversing system and the 3-axis model support. Wind tunnel reference data are required to ensure that the experiment is progressing properly. Data acquisition software has been developed which allows fully automated surveys of flowfields around models of arbitrary geometrical shape. A second computer system is required for data storing, reduction and processing by statistical means of the huge amount of data during instantaneous measurement cycles. This is done by online data transfer and communication with a CONVEX C1 and several work stations which ensure then a completely automatic process of flowfield measurements.

The model used is a very stiff model of a delta-canard configuration. A two-view sketch is presented in Fig. 1. For these tests, the canard setting angle has been fixed at 0 deg. The model was sting mounted on its lower surface by a computer controlled moving support strut providing an incidence range from 0 to 31.5 deg. This arrangement provides flowfield measurements to a great extent free from interference. The models may be yawed and banked up to 360 deg to ensure accurately positioning in the test section.

Hot-wire Anemometry

The hot-wire probes are operated by a DISA C three-channel constant-temperature anemometer system. Signal conditioner modules transform the bridge output voltages into a suitable range for the sixteen-channel simultaneous-sampling 12 bit A/D converter of the personal computer. The total sampling frequency is limited to 130 kHz. Cross-wire probes (DISA 55A32 and 55P61) were used to measure the magnitude and the associated direction of the time-dependent velocity vector. The sensors consist of 5-μm-diam platinum-plated tungsten wires giving a length/diameter ratio of 250. The wires form a measuring volume of approximately 0.8 mm in diam and 0.5 mm in height. The sensor angle of 45 deg was chosen assuming that the best angular resolution will be obtained with pairs of perpendicular wires. The signal of an additional temperature probe is used to correct the anemometer output-voltages analytically if ambient flow temperature varies.[27]

To calibrate the hot-wire probes a computer-aided fully automated procedure is developed based on a velocity- and flow angle dependent, temperature corrected method.[27-30] The use of a cross-wire configuration generally assumes some knowledge of the flowfield, such as a known flow direction to which the probe must be aligned. The nature of the vortex-dominated flow precludes any knowledge on the direction of the velocity vector everywhere in the field, save for the axial component which is assumed to be always in the positive x-direction. In order to fully determine all three velocity components (u, v, w) the probe has to be rotated around its axis by 90 deg to adjust the wire plane (once horizontal and once vertical) against the main flow direction. Thus, at least two traverse sweeps are necessary to obtain the streamwise (u), lateral (v) and vertical (w) components, respectively concerning the correction methods of Cutler and Bradshaw.[31]

Description of the Tests

Flowfield measurements were performed in a plane perpendicular to the model x-axis at a position where a single or twin-fin would be mounted, Fig. 2a,b. The tests were made for seven angles of attack (0, 15, 20, 25, 28, 30, 31.5 deg) and for two angles of sideslip (5, 10 deg). In order to analyze the vortex structure over the whole wing span a large survey plane was used at 15 and 30 deg angle of attack, Fig. 2b. The freestream reference velocity U_∞ was hold constant at 40 m/s. This gives a Reynolds number of approximately $Re = 1.0 \times 10^6$ based on the wing mean aerodynamic chord for all the results presented. Further test section conditions were ambient static pressure and temperature. As the wing leading-edge was sharp no transition strips were needed.

The sampling frequency for each anemometer channel was set to 3 kHz. The anemometer signals were low pass filtered at 1 kHz before digitization to counter the aliasing effect. This is due to the check that no other significant flowfield phenomena are present in the higher frequency domain. The sampling time for each measuring point is 26.4 s depending on stable, time-averaged auto-spectra of turbulent flow structures. The values based on random error evaluation methods[32] relate to an accuracy of 0.2%, 1% and 3% which are desired for mean and standard deviation and the spectral density, respectively.

$2s = 0.740$ m	$\varphi_W = 50°$
$l_\mu = 0.360$ m	$\varphi_C = 45°$
$\Lambda = 2.45$	$\lambda = 0.14$

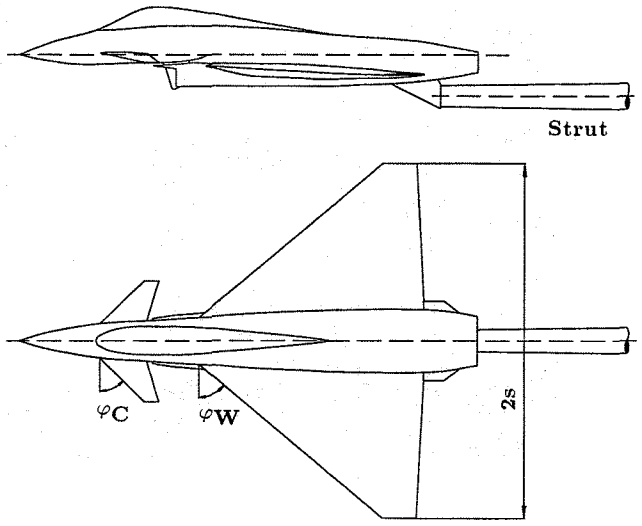

Fig. 1 Model of the delta-canard configuration.

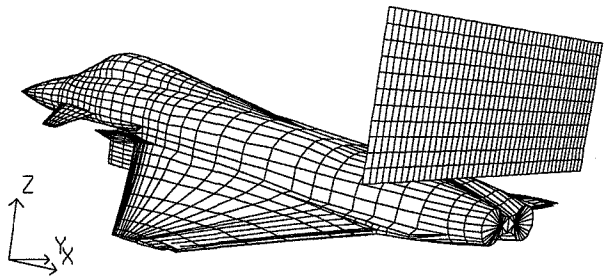

a) Standard plane

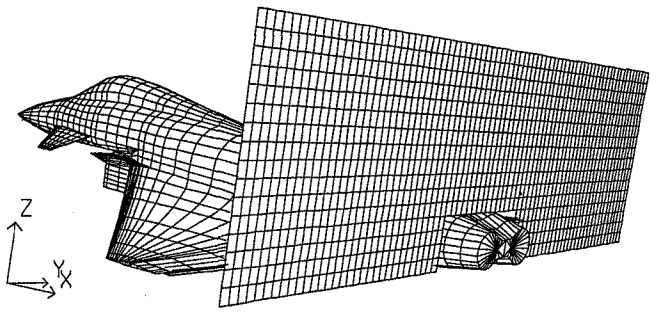

b) Large plane

Fig. 2 Location and discretization of the measurement plane.

The standard (large) survey plane contains 45 (77) evenly spaced points spanwise and 11 (16) evenly spaced points vertically, Fig. 2a,b. This gives a grid resolution of 0.014 in the spanwise and 0.020 in the vertical direction based on the wing span. The measurements were conducted with and without a single fin to get information about the influence of the fin itself on the formation of the vortex-dominated

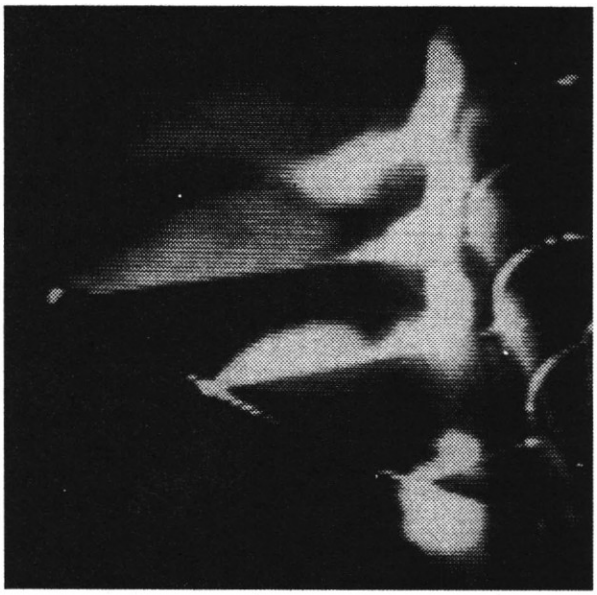

a) Delta–canard vortex system above the starboard wing (−Y); view from front

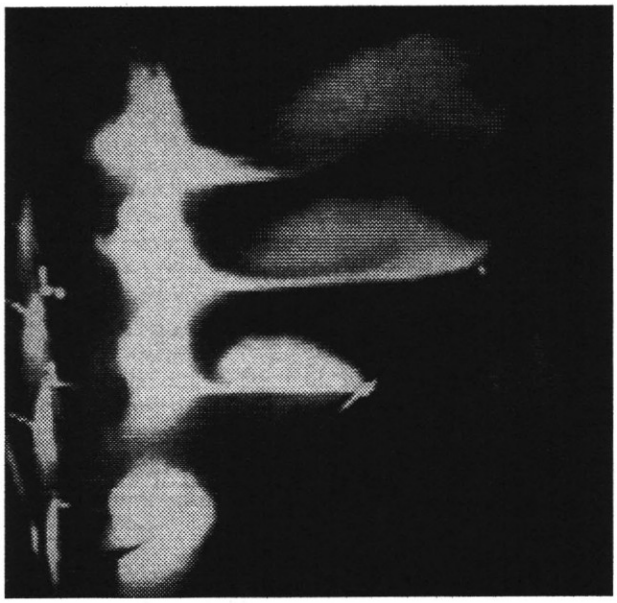

b) Delta–canard vortex system above the port wing (+Y); view from front

Fig. 3 Laser light sheet flow visualization at $\alpha = 15$, and $\beta = 5$ deg.

flowfield. Also the influence on the fin flow environment due to vortices emanating from small strakes mounted under the canopy was tested. Results given in this article are for the fin–off and strake–off case only. Ref. 33 contains the complete results of these investigations.

Results and Discussion

Flow visualization

Laser light sheet flow visualization were made to determine the evolution of the vortex systems, chiefly produced by the canard and the delta wing. Results shown here refer to four planes ($x/l_i = 0.3, 0.6, 0.85, 1.125$) over the delta wing at $\alpha = 15$ and $\beta = 5$ deg, Fig. 3a,b. The most downstream laser light sheet survey, located behind the wing at $x/l_i = 1.125$, corresponds to the mentioned hot–wire measurement plane, Fig. 2a,b.

At $x/l_i = 0.3$ the delta wing primary vortex on the leeward side (starboard wing) is bursted, Fig. 3a, whereas on the windward side (port wing), it is completely developed, Fig. 3b. At $x/l_i = 0.6$ the shape of the wing's leading–edge vortices becomes elliptically indicating the rapid expansion after vortex breakdown. A first bursting over the wing can be observed at $\alpha = 8$ deg. Bursting over the wing occurs on a simple 50–deg swept delta wing at $\alpha \geq 10$ deg. Because of the canard downwash, the wing leading–edge vortices develop progressively due to the lower effective angle of attack at inboard locations. At this model we have, however, a nonplanar wing which is strongly curved upwards near the fuselage. This is associated with an angle–of–attack increase in the region behind the canard. Thus, the canard downwash does not delay the vortex bursting over the wing. The less smoke intensity at downstream locations depicts the loss of vorticity in the bursted leading–edge vortices. From $x/l_i = 0.85$ the delta wing trailing–egde vortex can be detected which is completely rolled up and merged with the delta wing primary vortex in the last plane.

The canard vortex system consists of the canard's leading–edge and its trailing–edge vortex. Downstream the strong leading–edge vortex turns the trailing–edge vortex around in the sense of the rotation of the primary one. This vortex system keeps its structure downstream still behind the wing trailing–edge where the vortex shear layers of the canard and the wing vortex systems start to merge.[1]

In general, at a given angle of attack, sideslip effects a shift of the vortex systems in windward direction. In particular, on the leeward side both the delta–wing and the canard vortex systems are strongly moved inboard, Fig. 3a. On the windward side the vortex systems experience only a small displacement outboard, Fig. 3b. The fin region is, therefore, mainly influenced by the starboard delta–canard vortex systems.

Mean Velocity Distribution

Fig. 4 shows the cross flow velocity vectors at $\alpha = 15$, 30, and $\beta = 0, 5$ deg. It gives a general view about the development of the vortex–dominated flowfield from moderate to high angle of attack at symmetric and unsymmetric flow conditions. Contours of mean velocities $\overline{u}/U_\infty$, $\overline{v}/U_\infty$, $\overline{w}/U_\infty$ can be taken from Fig. 4 of Ref.1 and Fig. 5, respectively.

As found from the flow visualization tests the fin flow environment is affected by the interaction of the wing and canard vortex systems. At moderate angle of attack, $\alpha = 15$ deg, a distinctly swirling velocity field is evident indicating the wing vortex systems to be outboard and the canard vortex systems to be near the fuselage, Fig. 4a,b. At sideslip, the wing's port vortex system moves closer to its leading edge and remains concentrated whereas the starboard vortex system is enlarged and shifted to the fuselage. The canard's port vortex system moves outboard and downwards, the starboard one inboard and upwards, Fig 4b. This is a pure effect of the free flow directives.

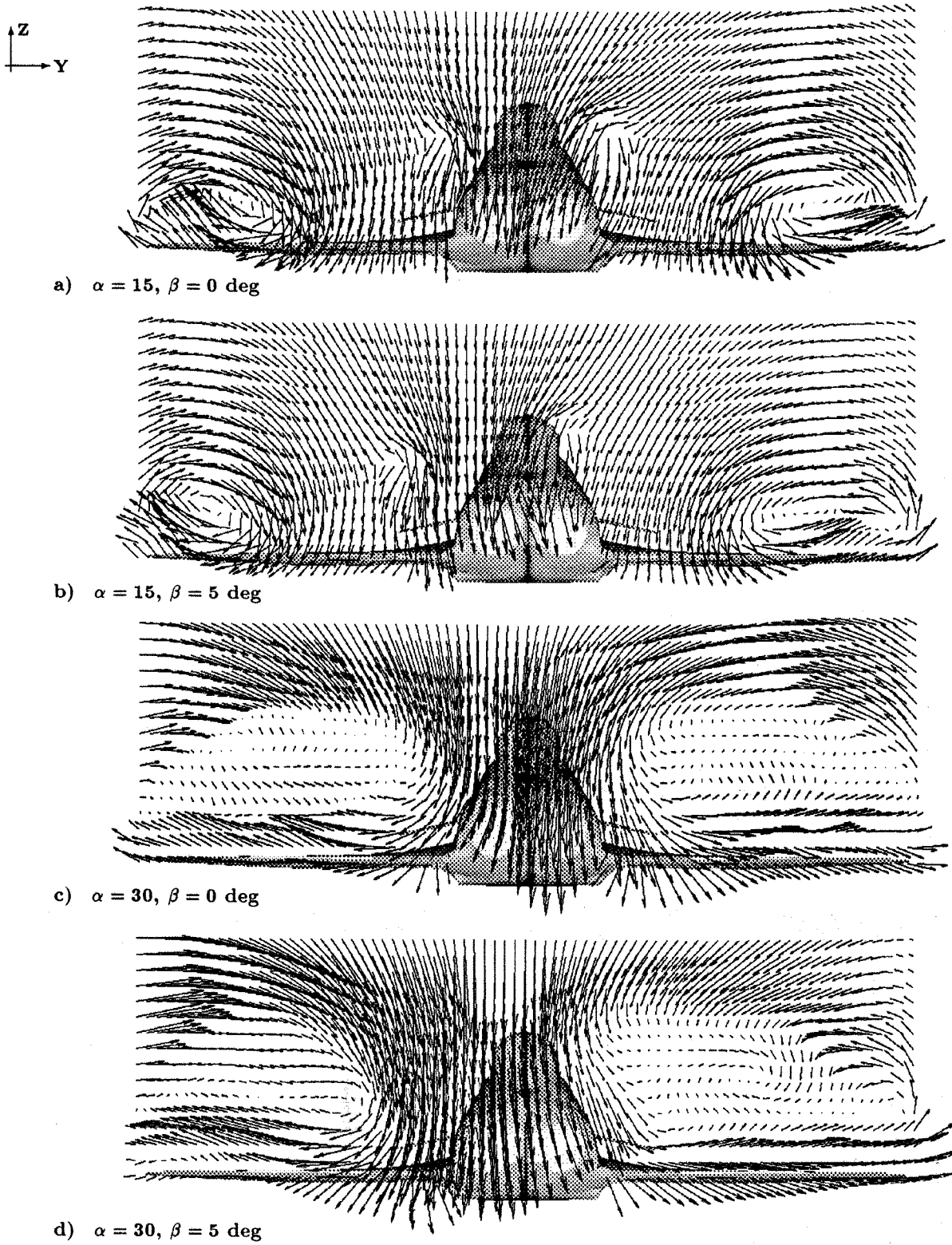

a) $\alpha = 15$, $\beta = 0$ deg

b) $\alpha = 15$, $\beta = 5$ deg

c) $\alpha = 30$, $\beta = 0$ deg

d) $\alpha = 30$, $\beta = 5$ deg

Fig. 4 Crossflow velocity vectors from moderate to high angle of attack at 0 and 5 deg sideslip.

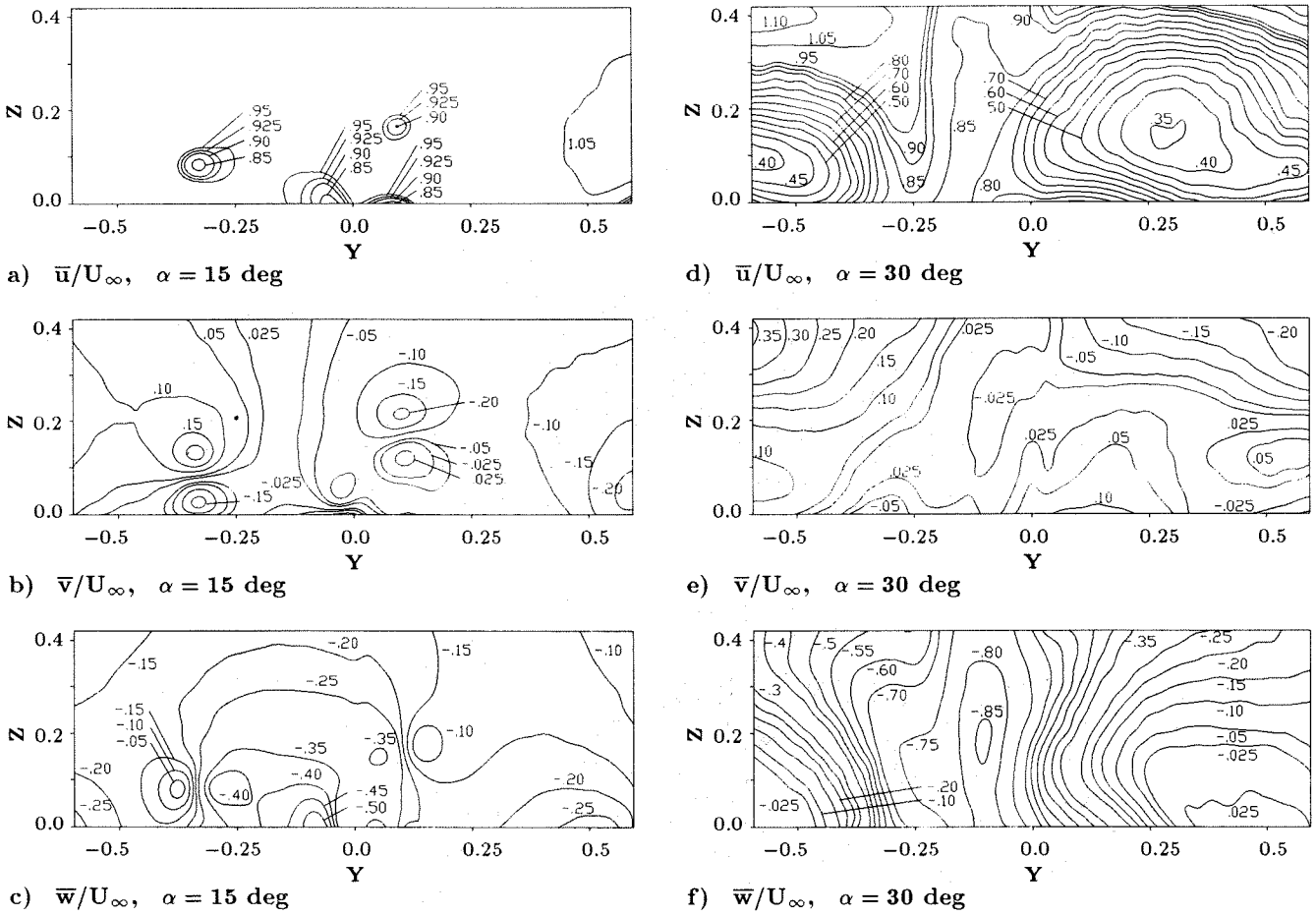

a) $\overline{u}/U_\infty$, $\alpha = 15$ deg

d) $\overline{u}/U_\infty$, $\alpha = 30$ deg

b) $\overline{v}/U_\infty$, $\alpha = 15$ deg

e) $\overline{v}/U_\infty$, $\alpha = 30$ deg

c) $\overline{w}/U_\infty$, $\alpha = 15$ deg

f) $\overline{w}/U_\infty$, $\alpha = 30$ deg

Fig. 5 Contours of mean velocity $\overline{u}/U_\infty$, $\overline{v}/U_\infty$, $\overline{w}/U_\infty$ at $\alpha = 15$, 30, and $\beta = 5$ deg.

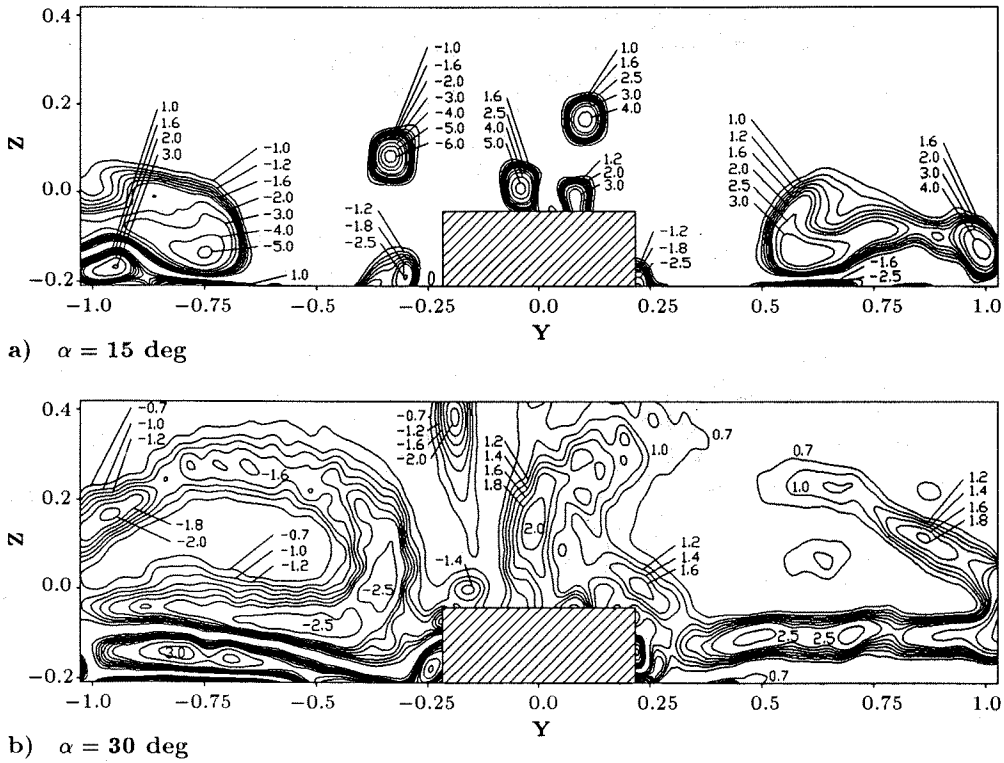

a) $\alpha = 15$ deg

b) $\alpha = 30$ deg

Fig. 6 Contours of axial vorticity Ω_X at $\alpha = 15, 30$, and $\beta = 5$ deg.

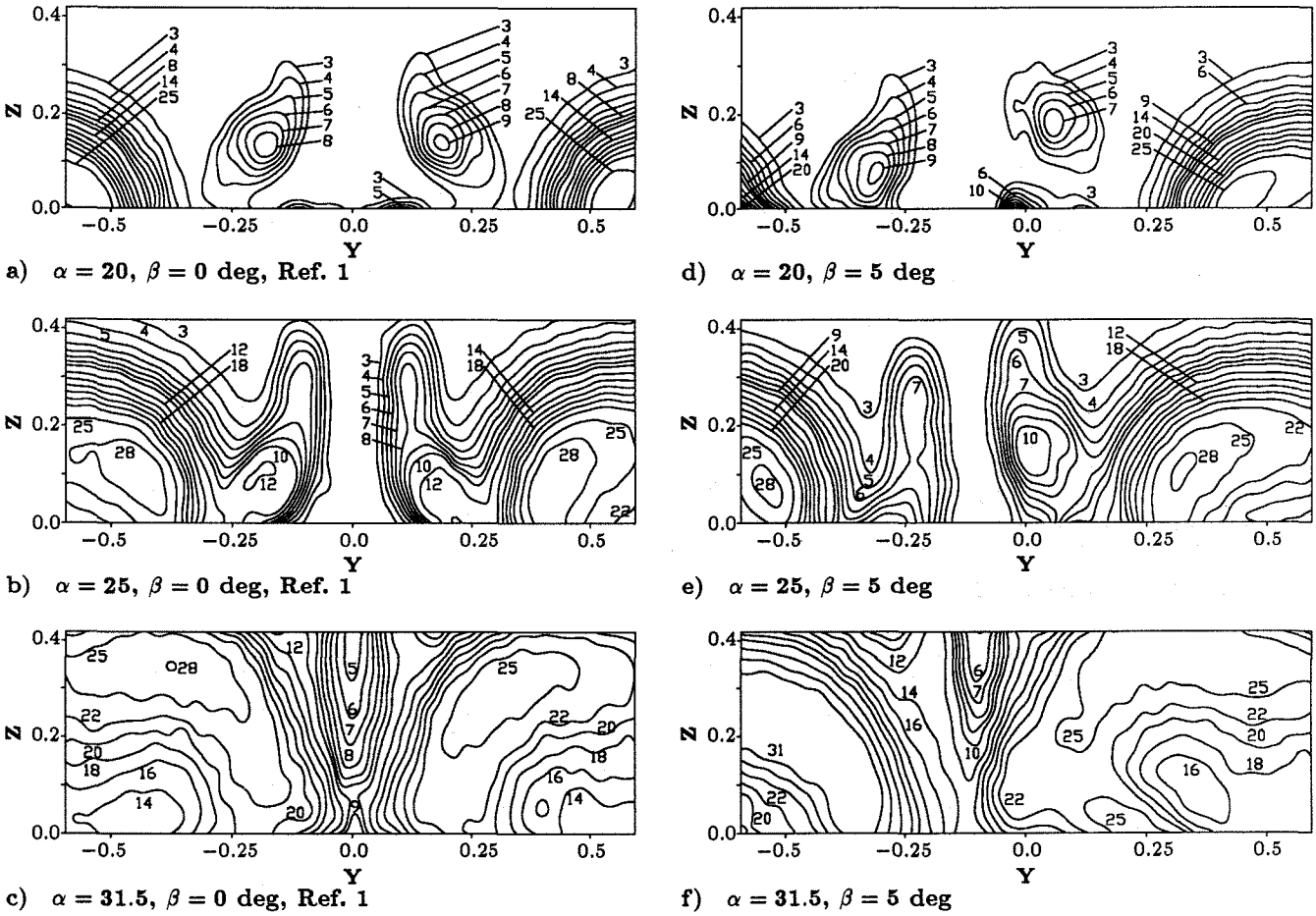

Fig. 7 rms velocity contours uxz_{rms}/U_∞ (sum of streamwise and vertical component) at $\alpha = 20, 25, 31.5$, and $\beta = 0, 5$ deg; (Values in percent).

The strong induction of additional spanwise and downward velocity predominates the cross–section. The local upwash from the canard vortex system is suppressed by the superimposed downwash field of the wing leading–edge vortices. Compared to $\beta = 0$ deg, the spanwise component in the mid section $\overline{v}/U_\infty$ has increased from 5% to 9%, Fig. 5b. A loss of axial and circumferential velocity is evident in the vortex cores. At the canard vortex systems this is qantified by an axial decelaration to 85% of the freestream value, Fig. 5a. Axial decelaration at $Z = 0, Y = \pm 0.05$ points out a further vortex pair which is shed at the canopy. It increases in strength, in particular, at sideslip. The considerable decrease of velocity in the vortex cores substantiates that even for moderate angles of attack the vortices are strongly influenced by viscous effects. Consequently the shape of the velocity field within the core is quite different from that of a potential vortex as expected.

At high angle of attack, $\alpha = 30$ deg, the flowfield is completely governed by the burst wing leading–edge vortices. They are emphasized by strongly enlarged core regions with severe flow decelaration, Fig. 4c,d. With increasing angle of attack the wing's primary vortices move inboard towards the fuselage and upwards above the wing. This is accompanied by an increase in intensity of the vortex induced cross–flow velocities outside the core. Because of the strong inward and downward velocity in the mid section the canard vortex system cannot be resolved any more. At $\beta = 5$ deg, the expansion of the vortex core stretches nearly to the mid section, Fig. 4d.

The growth of the vortex core is connected with the decrease of velocity to meet the continuity equation. It is obvious that strong viscous effects dominate the flow in a rather large area around the center of the primary vortex. Although the core becomes very large, a well–structured swirling flow pattern can be observed around it. The rapid change from flow acceleration to deceleration at the border of the vortex cores results in strong velocity gradients, Fig. 5d-f. The axial velocity $\overline{u}/U_\infty$ in the leeward wing vortex core has decelerated even to 35%, Fig. 5d; the spanwise and vertical component, $\overline{v}/U_\infty$, $\overline{w}/U_\infty$, show values of 2.5% – 5%, Fig. 5e,f.

When the angle of attack is further increased the borders of the primary vortices move closer together. The region centered between is characterized by a nozzle effect due to the induced circumferential velocities. At sideslip, Fig. 4d, this region is shifted from the mid section in windward direction.

Axial Vorticity

Central differencing of the velocity field is used to obtain the axial vorticity component Ω_x nondimensionalized by the wing span and the freestream velocity.

At 15 deg angle of attack, the resulting vorticity field in-

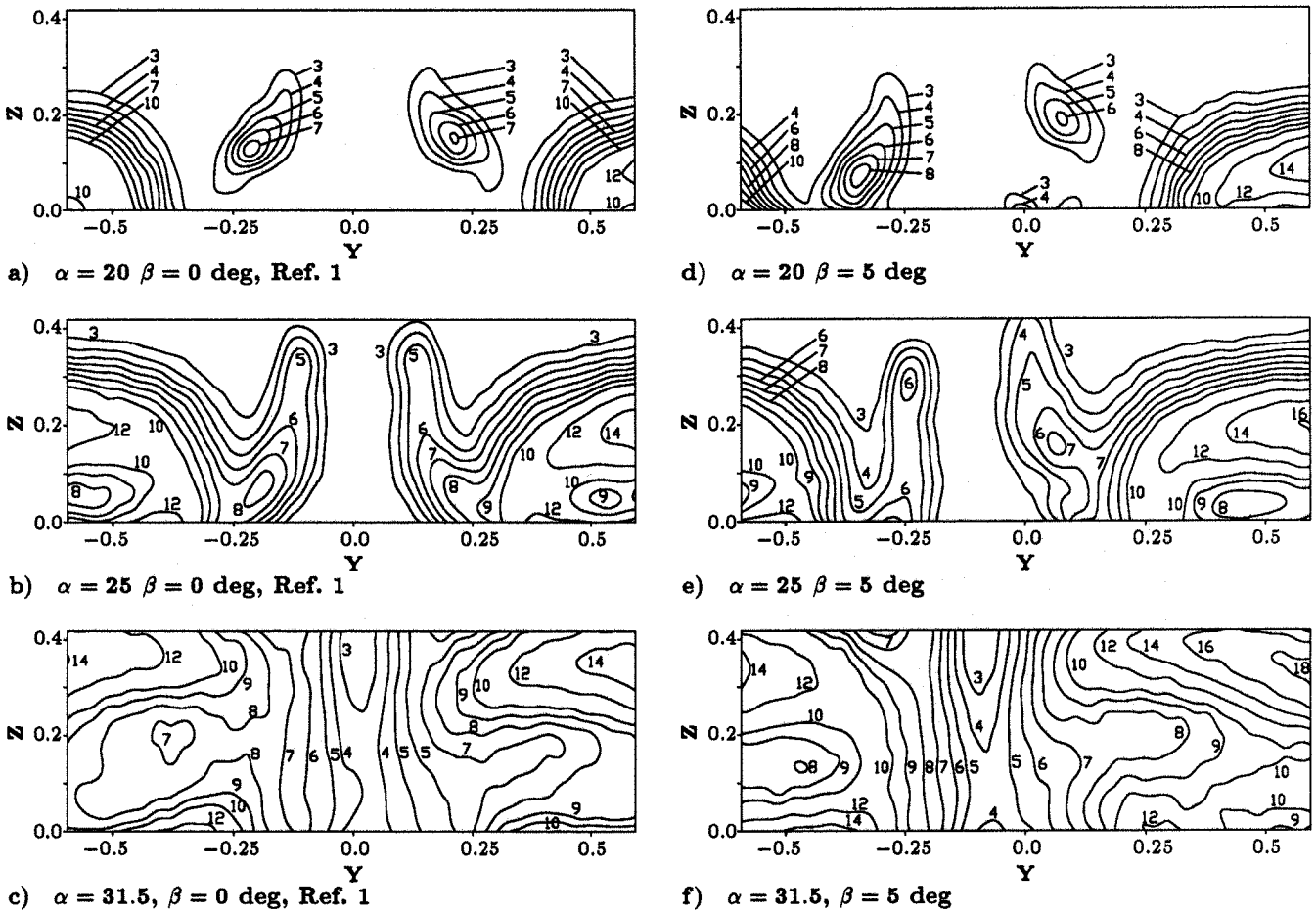

Fig. 8 rms velocity contours v_{rms}/U_∞ at $\alpha = 20, 25, 31.5$, and $\beta = 0, 5$ deg; (Values in percent).

dicates that the majority of axial vorticity is concentrated in the region immediately around the vortex cores, Fig 6a. Due to the increase in sweep angle of the port wing and the canard at sideslip the corresponding vortex systems show higher vorticity levels as the starboard vortex systems. At each side of the configuration regions with opposite sign of vorticity can be seen below the wing's primary vortex systems indicating secondary vortices. Furtheron vortices directly above and beside the fuselage are visible emanating from the canopy and from the undersurface wing–body junction, respectively.

As the angle of attack is increased to 30 deg the vorticity is mainly concentrated in the remaining swirling shear layer surrounding the strongly expanded vortex cores, Fig. 6b. The canard leading–edge vortices are completely merged within the the wing's primary vortices whereas the canard trailing–edge vortices are detached upwards. In particular, at sideslip a local maximum of vorticity is located in the mid section referring to the combined leeward delta–canard vortex sheets.

Root–mean–square Velocity Distribution

The turbulent flow structure is quantified by the root–mean–square values of the velocity fluctuations. Figs. 7 and 8 contain the rms contours, Fig. 9 presents carpet plots of the rms–distribution for all three velocity components.

Combined streamwise and vertical as well as lateral rms–distributions are shown in Figs. 7a,d and 8a,d for $\alpha = 20$, and $\beta = 0, 5$ deg. The canard leading–edge vortices are indicated by local rms maxima of approximately 8% - 10% around the mid section. The increase of axial and circumferential velocity on a line from above the vortices through their center is stopped at the border, where turbulence intensity starts to dominate the flow, Fig. 4,5. Beginning there, the velocity vector decreases while turbulence intensity increases as the center of a vortex is approached.

There is also an evident increase in turbulence intensity at the outer region of the measurement plane which are related to the wing primary vortex sheets as well as very steep gradients in the rms–distribution in the sheet itself. This corresponds to the sharply marked off vortex core of strong flow deceleration, Fig 5d. The maximum rms values reach levels of approximately 25%. At $\beta = 5$ deg, the leeward canard vortex system is located very close to the mid section. It results there in a noticeable increase in turbulence intensity even at moderate angles of attack.

At $\alpha = 25$ deg, Fig. 7b,e and 8b,e, the turbulent region has grown considerably in both size and strength due to vortex shift with angle of attack and the fusion of the canard and the wing vortex sheets. The lower part of the measuring plane is, therefore, dominated by large rms values for all three velocity components. In addition, sideslip causes that

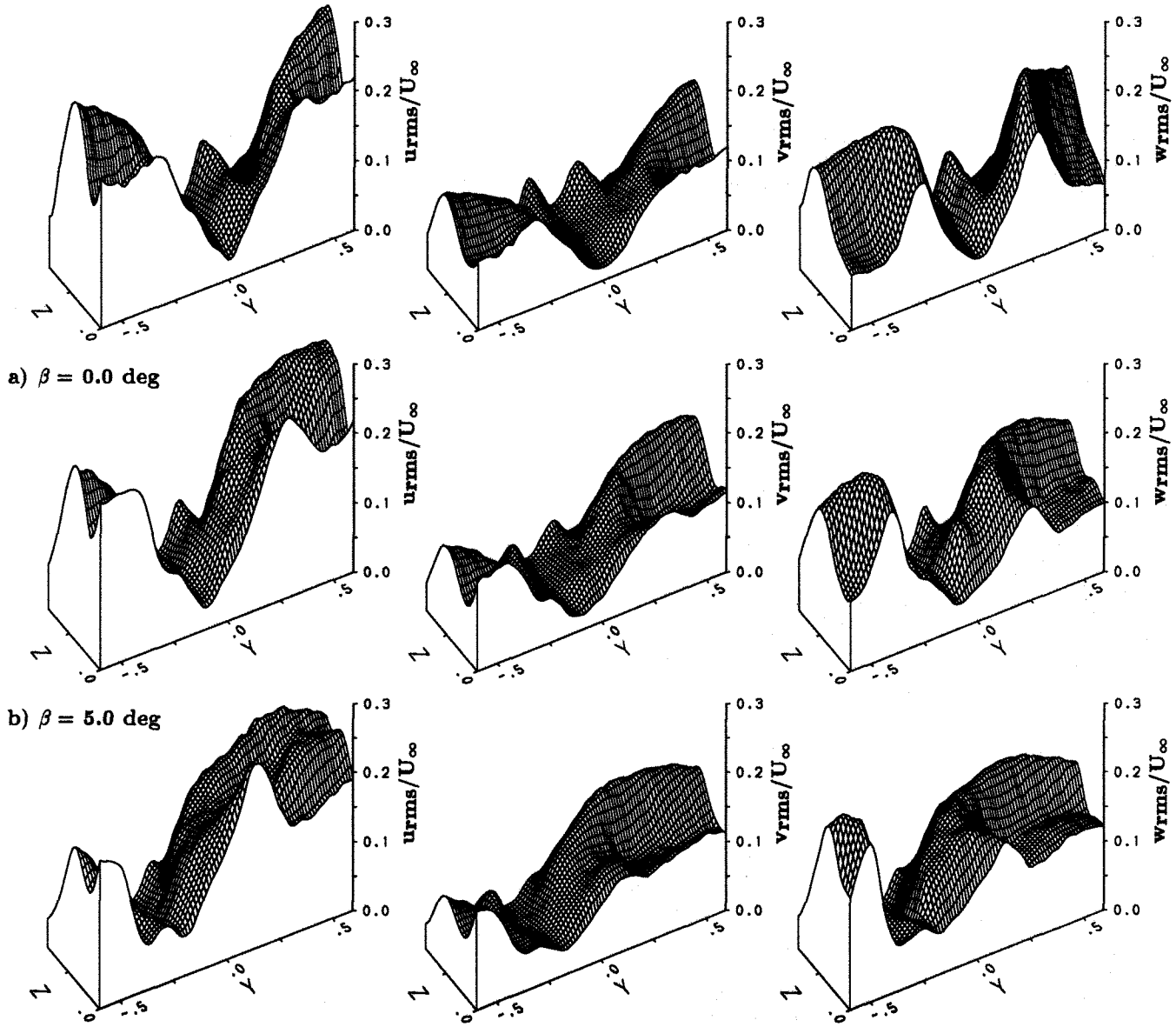

Fig. 9 Carpet plots of streamwise, lateral und vertical rms velocity, u_{rms}/U_∞, v_{rms}/U_∞, w_{rms}/U_∞, at $\alpha = 28$ deg.

the plane of symmetry is totally covered by the leeward canard vortex system. As mentioned before, the canard vortex system is indicated by local rms maxima near the mid section.

With increasing angle of attack the canard vortex system passes the wing leading-edge relatively high above the wing. From the comparison of Figs. 7a,d ($\alpha = 20$ deg) and Figs. 7b,e ($\alpha = 25$ deg) it can be inferred that through wing influence the canard vortex system is shifted above the wing inward towards the fuselage and also downward towards the wing surface. Going downstream the canard trailing-edge vortex turns around the canard leading-edge vortex both having the same sense of rotation, Fig. 3a,b. During this process the corresponding turbulent regions are spread out in the vertical direction, Fig. 7b,e. At 25 deg angle of attack the interaction between the vortex systems of the wing and the canard is such that the canard vortex sheet belonging to the trailing vortex starts to move upwards away from the wing while the canard leading-edge vortex is moved inwards and downwards to be merged within the sheets of the wing primary vortices.

With a further increase to $\alpha = 30$ deg, the rms values still rise, Figs. 7c,f, 8c,f. The maximum rms values have not grown considerably, but their region of influence has. The canard leading-edge vortices are completely combined with the wing leading-edge vortex sheets. The upper part of the canard's vortex system referring to the trailing-edge vortices remains separate from the wing's primary vortex sheets. The maxima of the rms velocity fluctuations go up to 31%, 15% and 28% for the u, v and w components, respectively. At $\beta = 5$ deg, values of 22% and 8% for the u and v component are present in the mid section. A reduction of turbulence due to flow acceleration between the two wing leading-edge vortices is seen.

The vortex regions of the wing primary vortices reveal that the maxima of the rms velocities are concentrated in an annular–like structure around the core, Fig. 9a–c. It is related to the vortex sheet due to the swirling pattern. The inner part of the core has, however, a decrease in local rms. The reason for lower rms values in the core is the loss of mean velocity as well as the low velocity gradient within the core. Thus, the turbulence level is reduced. This can be observed for all three velocity components. The very steep gradients of the vortex sheet's rms–distribution outside the core do not change with increasing angle of attack.

At increasing sideslip, Figs. 9b,c, the maximum rms values of the velocity fluctuations affect strongly the mid section caused by the inward shift of the leeward wing primary and combined canard vortex sheets. The severe increase of lateral rms velocity fluctuation in the mid section at high–α is significantly amplified at sideslip.

Fig. 10 presents the turbulence level of the v–component for a vertical mid–fin position in the plane of symmetry as a function of the angle of attack and sideslip. At symmetric flow conditions a significant rise starts at $\alpha = 25$ deg when the primary vortex approaches the plane of symmetry. The rms levels increase from 0.7% at $\alpha = 0$ deg to 4.5% at $\alpha =$ 31.5 deg. Sideslip effects that the sudden increase in local rms starts at lower angles of attack where both magnitude and gradient are strongly increased. At $\beta = 10$ deg the value of lateral rms rise to a level of 10.3% for $\alpha = 28$ deg.

By comparison with symmetric flow conditions where a centered single fin would be quite safe of buffeting,[1] the mid section of a configuration at sideslip do not longer show the lowest turbulence level. At sideslip the turbulent flow environment of a single–finned configuration may become comparable to that of a twin–finned configuration at symmetric flow.

Summarizing, Fig. 11 gives a schematic overview of the cross–sectional wing flowfield and its turbulence level at high angles of attack. They are shown for a spanwise and a vertical line through the vortex core. For moderate angles of attack ($\alpha \approx 15$ deg), the leading–edge vortices are concentrated outboard. The rms profiles show the two peaks corresponding to the vortex sheet and a local rms drop in the vortex core.[1] Steep gradients indicate the inboard and outboard vortex sheet. In the mid section the turbulence level is low also at sideslip. A fundamental change occurs in the flowfield if the angle of attack is increased to $\alpha \approx 30$ deg. The leading–edge vortices move inboard, accompanied by a strong expansion of the vortex core due to vortex burst. Thus, the turbulence levels are also markedly increased. At symmetric flow conditions the mid section remains, however, still the locus of minimum turbulence levels. At sideslip the mid setion is influenced by a strong increase in turbulence intensity due to the starboard shift of the enlarged vortex cores.

Spectral analysis

For a single fin mainly the lateral flowfield velocity causes buffeting, whereas for a twin–fin with dihedral both the lateral and the vertical velocity contribute. Spectral analysis gives the magnitude and the frequencies for the buffeting excitation levels.

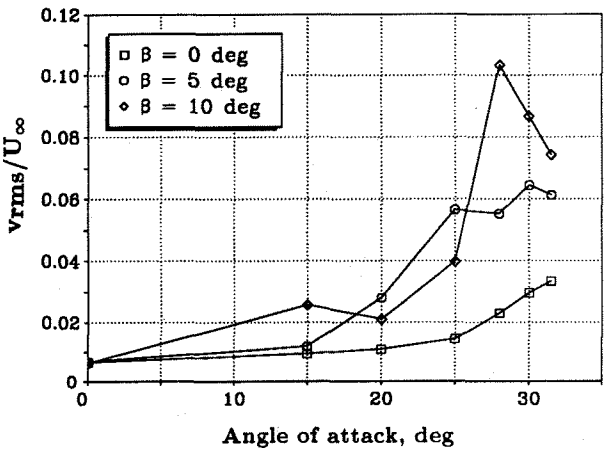

Fig. 10 Lateral rms velocity in the plane of symmetry as a function of angle of attack and sideslip at Z = 0.21.

Character of the Spectral Content at High Angle of Attack

Fig. 12 gives the stations for which the velocity spectra have been evaluated. Results shown for the lateral component v at $\alpha = 30$ deg only, give a general view of the distribution of kinetic turbulent energy at high–α due to sideslip. Six single density spectra plots and two staggered spectra plots both of the left and right side of the considered cross–dection are shown in Fig. 13.

The velocity spectra in Fig. 13a and Fig. 13d are related to mid–wing stations left and right of the plane of symmetry. The spectrum of the windward station 1l shows a distinct frequency peak at $k = 0.89$ caused by the influence of the outboard wing vortex sheet. At the leeward station 1r corresponding to the wing vortex core the spectrum has a pronounced and broad frequency hump ranging from $k = 0.52$ to $k = 1.16$. The turbulence level reaches values of 11.2% and 14.0% based on freestream velocity.

At station 2l, Fig. 13b, a strong narrow–band frequency peak which is closely associated with the pronounced velocity fluctuations of the inboard wing vortex sheet is observed. The turbulence level reaches values of approximately 10%. In comparison, the leeward station 2r, Fig. 13e, is mainly affected by the vortex core. This results in a spectrum with a broader frequency hump. From Figs. 13b and 13e it appears that the spectral energy is accumulated within a limited frequency band. It is distinctly small windward because of the vortex sheet influence and it is widened leeward because of the vortex core influence. This may indicate a periodic or quasiperiodic fluctuation. It is caused by the swirling vortex pattern. Roughly 75% – 80% of the turbulent energy is concentrated within this narrow band.

The spectral density for station 3l near the mid section is appreciably small, Fig. 13c. The kinetic turbulent energy decreases by an order of magnitude, but the spectra show a concentration of kinetic turbulent energy in the specified frequency range again. The narrow–band spectral density at the leeward station 3r remains relatively high because of the vortex shift at sideslip. It is obvious that at sideslip the vortex–induced concentration of turbulent energy into

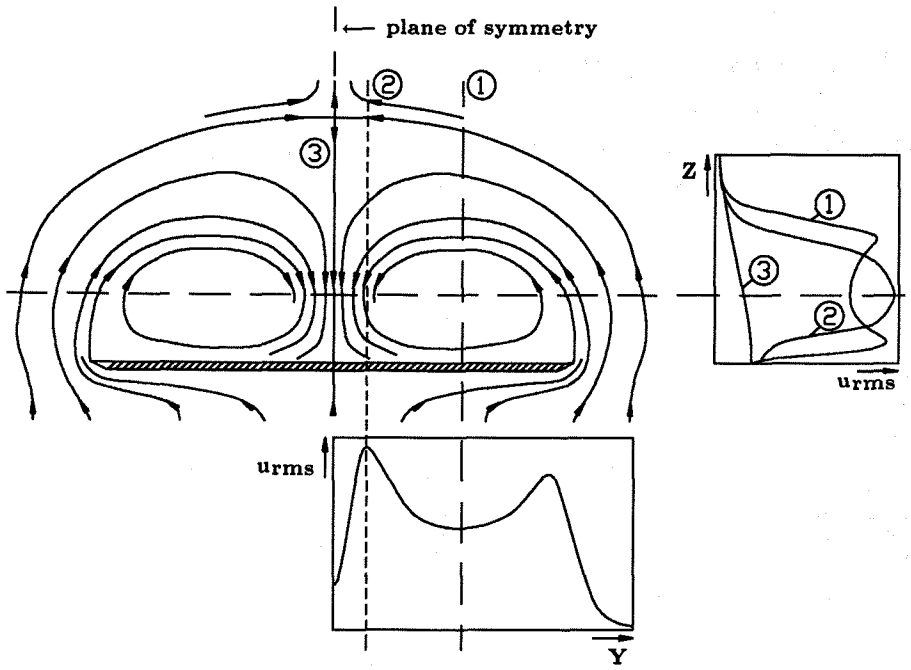

a) Transverse flowfield and rms profiles at $\alpha \approx 30$ deg and no sideslip

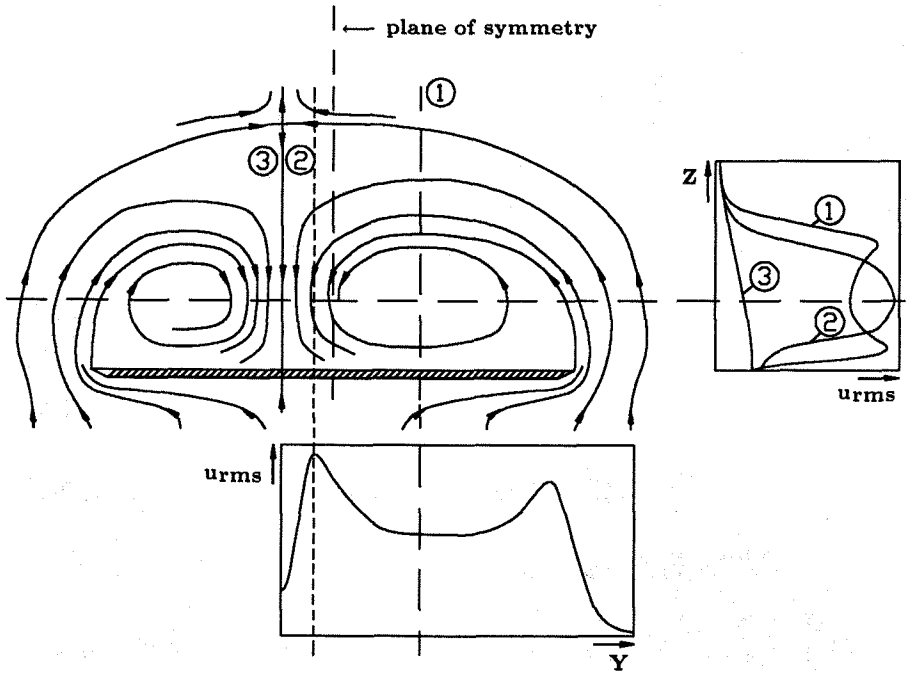

b) Transverse flowfield and rms profiles at $\alpha \approx 30$ deg and sideslip

Fig. 11 Schematic overview of the steady and unsteady flowfield velocity at high angle of attack and sideslip.

a limited frequency band affects the flow conditions in the plane of symmetry far more as at $\beta = 0$ deg. This results in a broader dominant frequency band and an amplified excitation level in the mid section.

Furtheron the power spectral density increases strongly in spanwise direction, Figs. 13g and 13h, what is directly related to the vortex shear layer and core position. The turbulent energy is mainly concentrated within $k = 0.62 \div 1.16$.

Variation of Frequency Content with Angle of Attack

Fig. 14 shows spectra for various angles of attack and sideslip at station 4 (plane of symmetry). Up to 20 deg, Fig. 14a, a broadband spectrum may excite normal, random buffeting. From Figs. 7a and 8a it can be derived, that no vortex sheet influences the mid section at that angle of attack. At $\alpha = 25$ deg, the spectral content becomes quite different. At $\beta = 0$ deg, Fig. 14b shows a spectrum

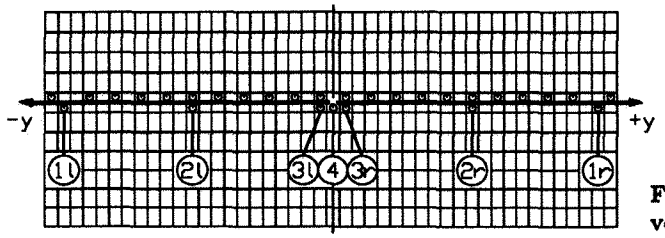

Fig. 12 Measurement stations for velocity spectra.

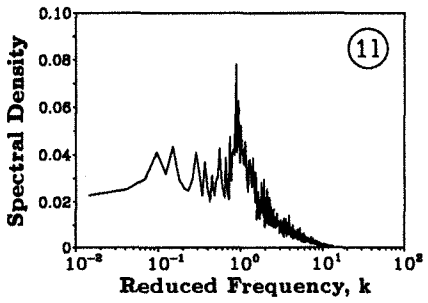

a) Station 1l, $v_{rms}/U_\infty = 11.2\%$

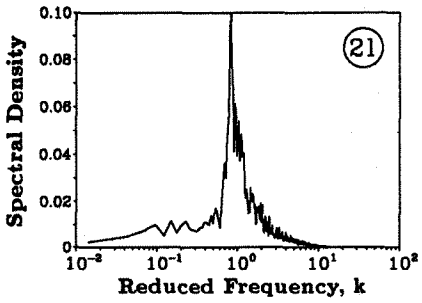

b) Station 2l, $v_{rms}/U_\infty = 9.4\%$

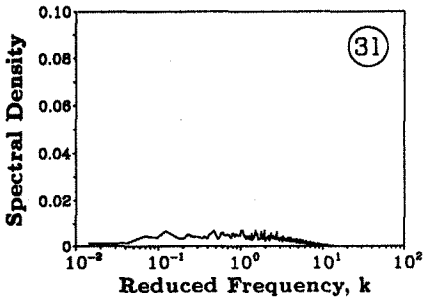

c) Station 3l, $v_{rms}/U_\infty = 5.5\%$

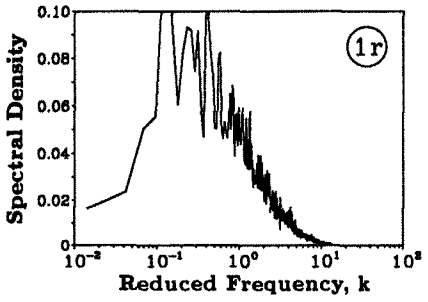

d) Station 1r, $v_{rms}/U_\infty = 14.0\%$

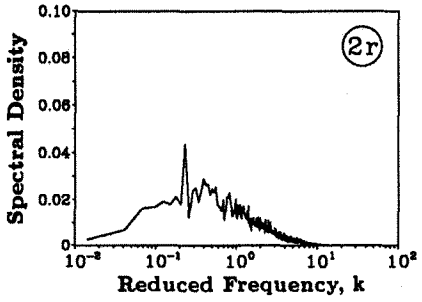

e) Station 2r, $v_{rms}/U_\infty = 8.1\%$

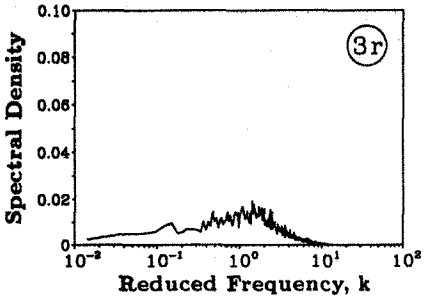

f) Station 3r, $v_{rms}/U_\infty = 7.7\%$

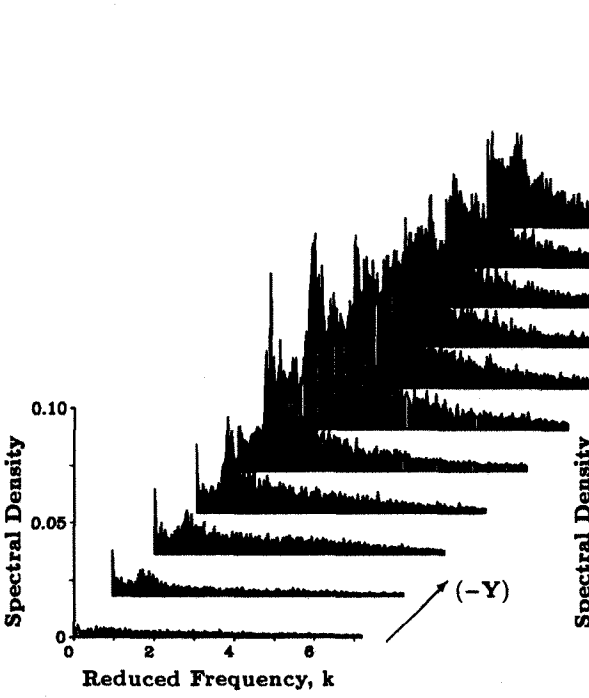

g) Spectra of the left side (−Y)

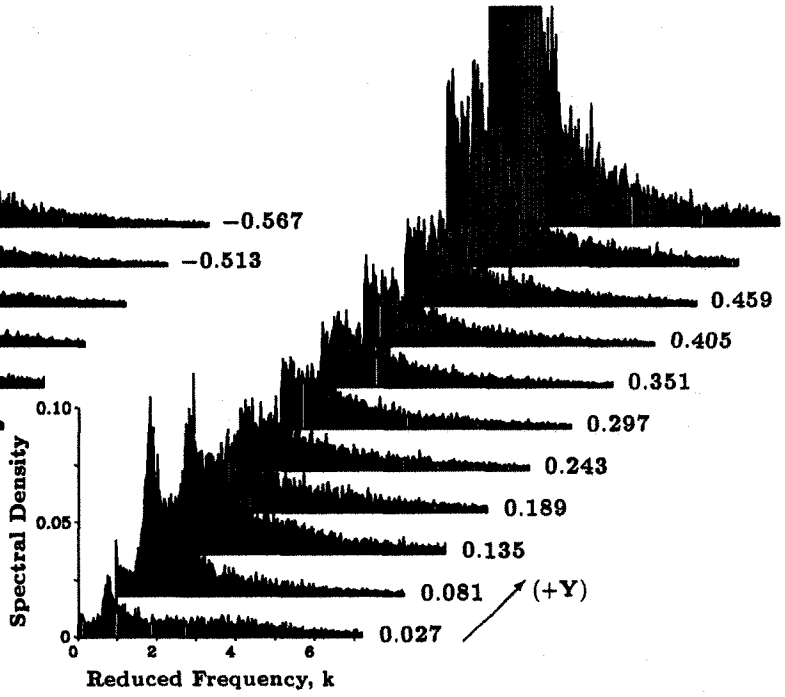

h) Spectra of the right side (+Y)

Fig. 13 Spectra of the lateral velocity component v, left and right of the plane of symmetry at Z = 0.21, and $\alpha = 30$, $\beta = 5$ deg.

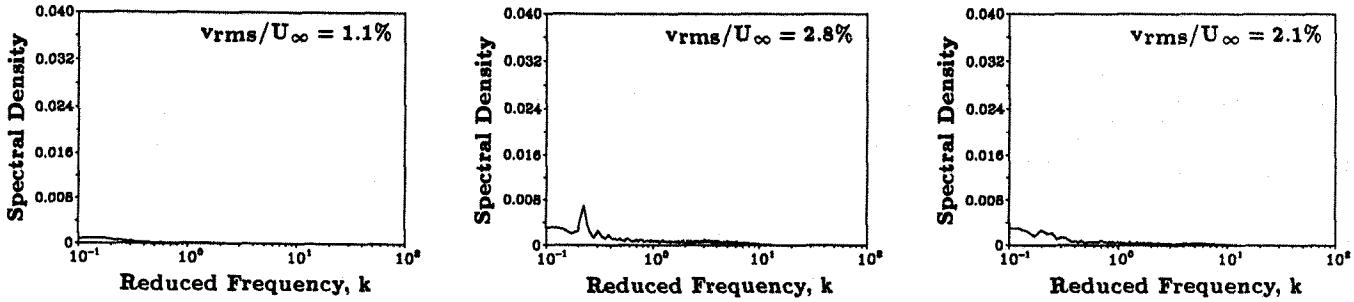

a) $\alpha = 20.0$, $\beta = 0.0$ deg $\quad$ $\beta = 5.0$ deg $\quad$ $\beta = 10.0$ deg

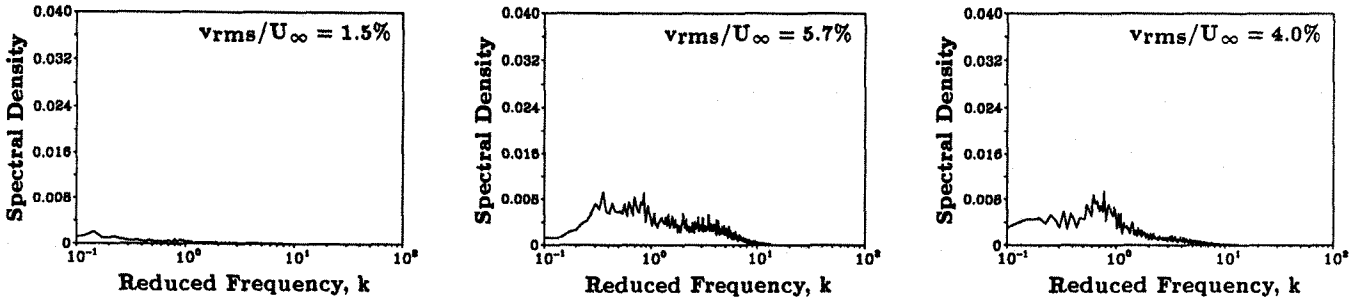

b) $\alpha = 25.0$, $\beta = 0.0$ deg $\quad$ $\beta = 5.0$ deg $\quad$ $\beta = 10.0$ deg

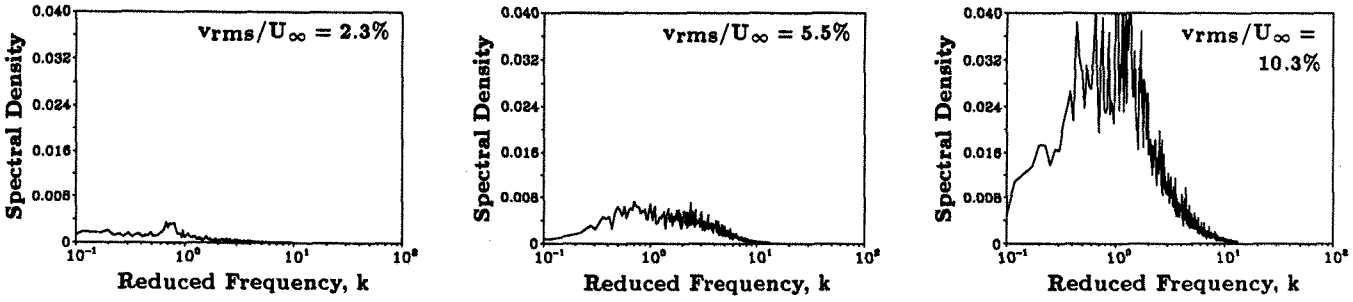

c) $\alpha = 28.0$, $\beta = 0.0$ deg $\quad$ $\beta = 5.0$ deg $\quad$ $\beta = 10.0$ deg

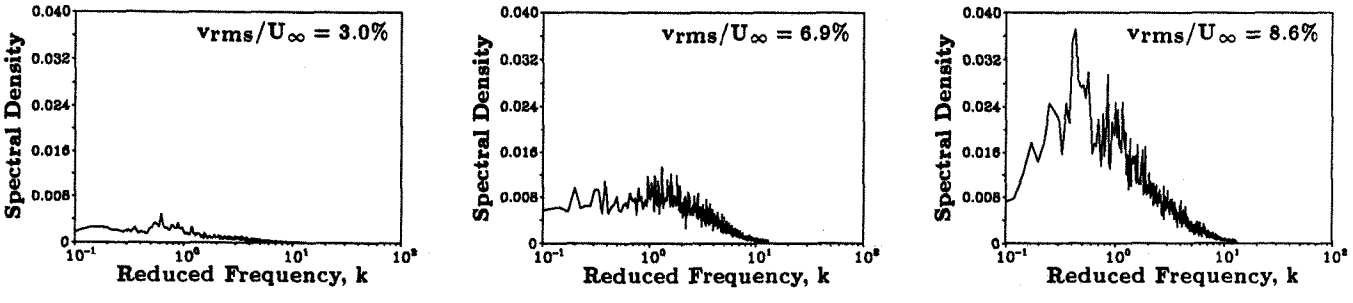

d) $\alpha = 30.0$, $\beta = 0.0$ deg $\quad$ $\beta = 5.0$ deg $\quad$ $\beta = 10.0$ deg

Fig. 14 Spectra of the lateral velocity component v at station 4 (plane of symmetry, Z = 0.21) for various angles of attack and sideslip.

with low turbulence level, but sharp peaks occur around a hump of $k = 0.9$, Ref. 1. A strong increase in the excitation level appears at $\beta = 5$ and 10 deg when the combined leeward delta–canard vortex sheets hit the plane of symmetry. For the mid section the dominant frequency hump cannot be detected at a lower angle of attack.

A dramatic change occurs for the spectral density at $\alpha = 28$ deg, Fig. 14c. At $\beta = 0$ deg, a distinct narrow-band frequency peak centered around $k = 0.75$ predominates the whole spectrum. At $\beta = 5$ deg the peak becomes widened and the spectral density increases to twice the level of symmetric flow. The spectrum depicts a second pronounced peak around $k = 1.3$ which refers to the canard vortex system. During the merging process of the wing and the canard vortex sheets both vortex burst frequencies are dominant.

The channelization of spectral energy into a narrow band, Fig. 14b,c, corresponds with the sharp and broad frequency peak of the vortex sheet and core spectra which are discussed in Figs. 13b and 13e, respectively. At $\alpha = 30$ deg, Fig. 14d, the spectrum becomes widened around $k = 0.68$ also at $\beta = 0$ deg showing multiple peaks. At $\beta = 5$ and 10 deg, again a severe increase in spectral density is evident.

In the high–α domain the narrow–band concentration of kinetic turbulent energy according to the strong fluctuation intensity in the joined vortex sheets of wing and canard is extended to the plane of symmetry. This is caused by the inboard leading–edge vortex shift together with the growth of burst vortices, Figs. 7e,f and Figs. 8e,f. In the plane of symmetry a severe increase of the excitation level is present at sideslip flow conditions due to the additional windward vortex shift.

In Fig. 15, the velocity spectra for 10 deg angle of sideslip (Figs. 14a–d) are plotted together. With increasing angle of attack the frequency of the dominant peak(s) decrease. This effect due to the larger diameter of the burst vortex core with increasing incidence was also observed at zero sideslip.[1] This is substantiated in Fig. 16 showing an identical relationship between k and α at $\beta = 0$ and 10 deg. Beside the dominant frequency related to the wing vortex system also the frequency according to the canard vortex system is plotted over α becoming dominant at sideslip. Even using a linear scale, there is some ambiguity in the determination of the dominant peak because of single spikes centered around a broader hump. As observed previously[8,25] at different angles of attack the peaks of the buffeting spectrum may move into the range of different structural modes, resulting in a "tuning" of the vibrations. This is because of the fluctuations associated with the bursting of strong leading–edge vortices.

Reduced Frequency Scaling

Results for the delta–canard dominant frequency at 28–deg angle of attack are compared with data from various sources, Fig. 17. The latter were obtained by hot-wire/film and accelerometer measurements near the vertical fin of F–15 aircraft models and the fullsize airplane at 20–deg angle of attack. At this incidence a distinct spectral peak was observed. In detail, Ref. 19 shows data from hot–film measurements in the vicinity of the vertical tails of small– and large–scale models at low speed. Ref. 20 mentions hot–wire tests performed near both a rigid vertical tail model as well as an aeroelastically scaled model in a low speed wind tunnel. Ref. 20 provide additional data of the acceleration spectrum at the top of the left vertical tail, measured during flight test of the full–scale airplane. This spectrum exhibits a dominant frequency.

A good correlation is evident between the reported data and the data given in the literature. Data from rigid models, elastic models and the full–scale vehicle are included. The data span 3 orders of magnitude in Reynolds number and ranges from Mach 0.05 to Mach 0.6. The dynamic pressure ranges from 32.08 N/m^2 to 11395 N/m^2. The relation between the reduced frequency and freestream velocity is seen to be linear. The reduced frequency averaged over the delta–canard data at different velocities is 0.73. The am-

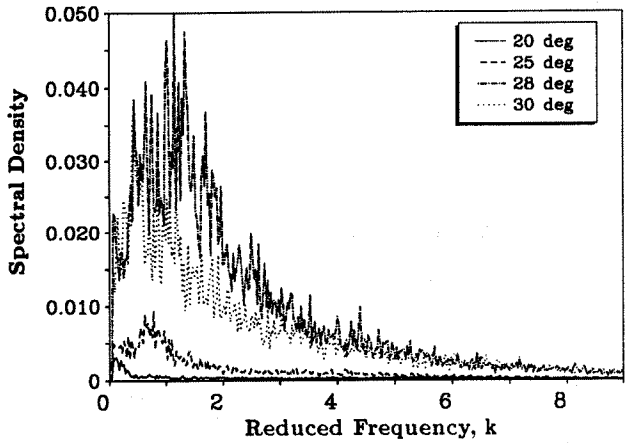

Fig. 15 Comparison of the v–velocity spectra at station 4 (plane of symmetry, Z = 0.21) for various angles of attack at $\beta = 10$ deg.

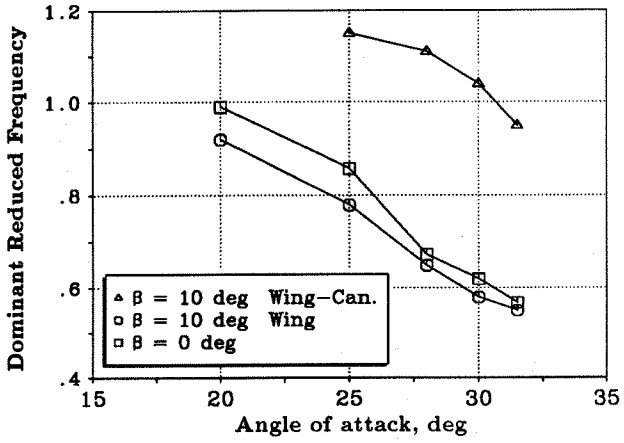

Fig. 16 Reduced frequency of dominant spectral peaks as a function of angle of attack, measured at station 4 (plane of symmetry, Z = 0.21).

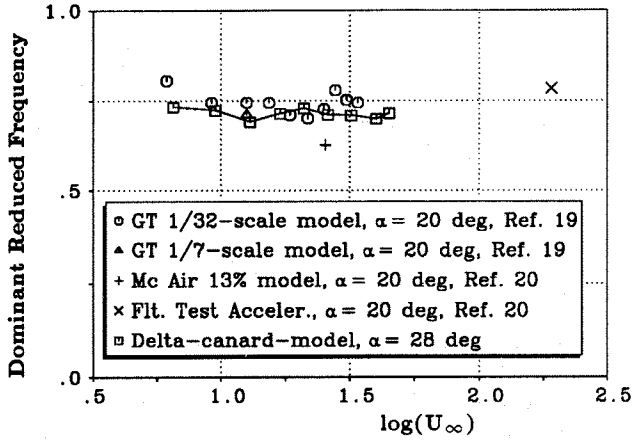

Fig. 17 Strouhal scaling of the dominant spectral peak based on data from hot-wire/film anemometry and flight test accelerometer measurements.

plification of the excitation level reaches a factor of 5 at $\beta = 10$ deg ! A single fin would be then completely surrounded by the leeward delta–canard vortex sheets encountering heavy buffeting.

The average over the 1/32 and 1/7 GT data is 0.74, the flight test point is 0.78, and the McAir 13% model result is 0.62. This provides strong evidence that in modeling the frequency of the strongest tail vibrations, Reynolds number and Mach number matching are not of primary importance. Of course the latter parameters are important for modeling the detailed flow over the panels of a vertical tail itself.

Variation of Fluctuation Amplitude

Fig. 18 plots the lateral rms velocity v_{rms}/U_∞ at station 4 (plane of symmetry) against the freestream velocity ($\beta = 0$ deg). It is seen that the relation between nondimensionalized turbulence intensity and freestream velocity is fairly linear over the considered velocity range. The level of turbulence intensity increases with angle of attack reaching a maximum at $\alpha = 31.5$ deg where the rms is of the order of 4.5%. Sideslip presents similar results amplifiing the maximum rms level to 6.3% at $\beta = 5$, $\alpha = 30$ deg and 10.2% at $\beta = 10$, $\alpha = 28$ deg.

The variation of the spectral density of the dominant peak with freestream velocity shows a strong increase of the fluctuation amplitude of the dominant peak with freestream velocity, Fig. 19. Again, the relationship seems to be nearly linear over the shown velocity range.

Scaling to Full Scale

Using the reduced frequency k, the dominant peak can be scaled to full scale. The assumption would be, that leading–edge flow separation line is fixed and consequently not very much dependent on Reynolds number. As substantiated in Figs. 18 and 19, also nondimensionalized turbulence intensity as well as the spectral density of the dominant peak can be scaled to full scale.

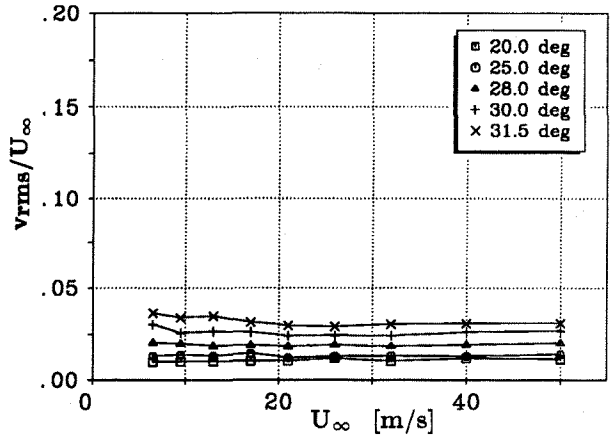

Fig. 18 Variation of nondimensionalized lateral rms velocity with freestream velocity, measured at station 4 (plane of symmetry, Z = 0.21).

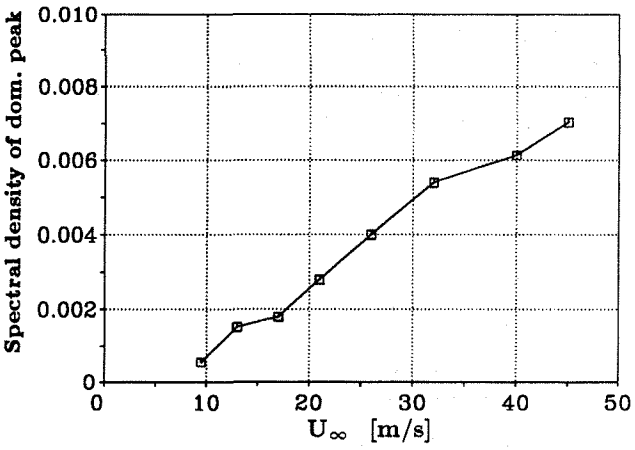

Fig. 19 Variation of spectral density of the dominant peak with freestream velocity, measured at station 4 (plane of symmetry, Z = 0.21) at $\alpha = 28$ deg.

Conclusions

The time–averaged, root-mean-square and frequency content of the velocity components in a turbulent flowfield caused by a vortex–dominated configuration have been studied from moderate to high angles of attack at sideslip. Hot–wire anemometry were used. Prime results of these investigation are as follows:

1) With increasing angle of attack, the delta–wing vortex systems move inboard towards the mid section and upwards. The vortices are continously expanded caused by a large vortex core due to burst. This is emphasized by a strong decrease of axial- and circumferential velocity.

2) At sidelip the wing and canard vortex systems are shifted outboard and downwards at the windward wing and inboard and upwards at the leeward wing. Thus the mid section is strongly affected by the leeward delta–canard vortex systems.

3) The burst vortex flowfield shows a strong increase of the turbulence level for all three velocity components. Steep gradients separate the vortex sheet region from the outer flowfield. The maxima of rms values shows an annular structure which are assigned to the vortex sheet while in the vortex core a local rms decrease occurs.

4) For moderate angles of attack ($\alpha < 20$ deg) it is shown that above the wing through wing influence the canard vortex system is moved towards the mid section and also downward towards the wing. At an angle of attack $\alpha \approx 20$ deg and at sideslip the interaction between the wing and the canard vortex systems makes the canard trailing–vortex sheet to move upwards whereas the canard leading–edge vortex sheet merges with the wing primary vortex. At the leeward side a local maximum in the turbulence level is found near the root of a possible single fin.

5) The spectra of the vortex sheets show a distinct narrow–band peak whereas the vortex core region reveals a broader frequency hump. The narrow–band concentration of kinetic turbulent energy indicates a strong periodicity in the flow.

6) At high angle of attack this narrow–band turbulent energy affects the plane of symmetry because of vortex shift and enlarged vortex cores. In the mid section sideslip effects the presence of a broader frequency peak as observed

at symmetric flow due to the influence of the leeward wing/canard vortex cores. In addition, a severe amplification in the excitation level up to 5 times against symmetric flow is encountered.

7) Depending on the angle of attack the frequency of the peak and the shape of the spectrum is changed.

8) Vortex–induced turbulence intensity as well as the reduced frequency of the dominant peak can be scaled to full scale.

9) At no sideslip conditions a single fin would be quite safe of buffeting. For unsymmetric flow conditions a single fin may be exposed, however, to a buffeting excitation level comparable with that of a twin–fin arrangement at no sideslip depending on the yaw angle. It is thought that the present investigation will give useful advice to this question.

Acknowledgements

This work was supported by Deutsche Aerospace under the directorat of Dr.-Ing. W. Schmidt. The authors express their appreciation to Dr.-Ing. J. Becker (DASA) for initiating the investigation and for his continuous advice and kind assistance.

References

[1] Breitsamter, C., and Laschka, B., "Turbulent Flow Structure Associated with Vortex-Induced Fin Buffeting," *Journal of Aircraft*, Vol. 31, No. 4, July-Aug. 1994.

[2] Lee, B. H. K., Brown, D., Zgela. M., and Poirel, D., "Wind Tunnel Investigations and Flight Tests of Tail Buffet on the CF–18 Aircraft," AGARD–CP–483, Aircraft Dynamic Loads due to Flow Separation, Sorrento, Italy, April 1990, pp. 1-1 – 1-26.

[3] Hebbar, S. K., Platzer, M. F. and Liu, D.-M., "Effect of Canard Oscillations on the Vortical Flowfield of a X–31A–Like Fighter Model in Dynamic Motion," AIAA–93–3427–CP, AIAA Applied Aerodynamics Conf., Monterey, CA, Aug. 1993, Part 1, pp. 241 – 250.

[4] Becker, J., "Bewegungsinduzierte Luftkräfte bei abgelöster Strömung und ihre Übertragung auf die Ermittlung der Strukturresponse," Ph.D. thesis, Technische Universität Braunschweig, Braunschweig, 1982.

[5] Ashley, H., Rock, S. M., Digumarthi, R. V., Chaney, K. and Eggers, Jr., A. J. "Active Control for Fin Buffet Allevation", WL–TR–93–3099, Flight Dynamics Directorate, Wright Laboratory, Wright Patterson AFB, OH, Jan. 1994.

[6] Mabey, D. G., and Pyne C. R., "Fin Buffeting at High Angles of Incidence on a Model of Slender Wing Aircraft," International Forum on Aeroelasticity and Structural Dynamics, Aachen, Germany, June 1991, Paper 91-129, 1991, pp. 552 – 561.

[7] Triplett, W. E., "Pressure Measurements on Twin Vertical Tails in Buffeting Flow," *Journal of Aircraft*, Vol. 20, No. 11, 1983, pp. 920 – 925.

[8] Wentz, W. H., "Vortex–Fin Interaction on a Fighter Aircraft", AIAA-87-2474, AIAA 5th Applied Aerodynamics Conf., Monterey, CA, Aug. 1987.

[9] Lee, B. H. K., and Brown, D., "Wind-Tunnel Studies of F/A–18 Tail Buffet," *Journal of Aircraft*, Vol. 29, No. 1, 1992, pp. 146 – 152.

[10] Brown, D., Lee, B. H. K., and Tang A., "Some Characteristics and Effects of the F/A–18 Lex Vortices," AGARD–CP–494, Vortex Flow Aerodynamics, Scheveningen, The Netherlands, Oct. 1990, pp. 30-1 – 30-20

[11] Lee, B. H. K., and Tang, F. C., "Unsteady Pressure and Load Measurements on a F/A–18 Vertical Fin," *Journal of Aircraft*, Vol. 30, No. 5, 1993, pp. 228 – 234.

[12] Martin, C. A., Glaister, M. K., Mac Laren, L. D., Meyn, L. A., and Ross, S., "F/A–18 1/9th Scale Model Tail Buffet Measurements," Aeronautical Research Lab. Flight Mechanics Rept. 188, June 1991.

[13] Lee, B. H. K., and Tang, F. C., "Characteristics of the Surface Pressures on a F/A–18 Vertical Fin Due to Buffet," *Journal of Aircraft*, Vol. 31, No. 1, 1994, pp. 228 – 234.

[14] Lee, B. H. K., Brown, D., Tang, F. C., and Plosenski, M., "Flowfield in the Vicinity of an F/A–18 Vertical Fin at High Angles of Attack," *Journal of Aircraft*, Vol. 30, No. 1, 1993, pp. 69 – 74.

[15] Erickson, G. E., Hall, R. M., Banks, D. W., Del Frate J. H., Schreiner, J. A., Hanley, R. J., and Pulley, C. T., "Experimental Investigation of the F/A–18 Vortex Flows at Subsonic Through Transonic Speeds, Invited Paper," AIAA Paper 89-2222, July 31 - August 2, 1989.

[16] Breitsamter, C., and Laschka B., "Velocity Measurements with Hot–Wires in a Vortex–Dominated Flowfield," AGARD–CP–535, Wall Interference, Support Interference and Flow Field Measurements, Brussels, Belgium, Oct. 1993, pp. 11-1 – 11-13.

[17] Sellers, W. L., Meyers, J. F., and Hepner, T. E., "LDV Surveys Over a Fighter Model at Moderate to High Angles of Attack," Society of Automotive Engineers TP Series Paper 88-1448, Oct. 1988.

[18] Komerath, N. M., Liou, S. G., Schwartz, R. J., and Kim, J. M., "Flow over a Twin–Tailed Aircraft at Angle of Attack, Part I: Spatial Characteristics", *Journal of Aircraft*, Vol. 29, No. 3, 1992, pp. 413 – 420.

[19] Komerath, N. M., Liou, S. G., Schwartz, R. J., and Kim, J. M., "Flow over a Twin–Tailed Aircraft at Angle of Attack, Part II: Temporal Characteristics", *Journal of Aircraft*, Vol. 29, No. 4, 1992, pp. 553 – 558.

[20] Colvin, B. J., Mullans, R. E., Paul, R. J., and Ross, H. N., "F–15 Vertical Tail Vibration Investigations," McDonnell–Douglas Corporation Rept. A6114, McDonnell Aircraft Company, St. Louis, MO, Sept. 15, 1979.

[21] Bean, E. B., Greenwell, I. D., and Wood N. J., "Vortex Control Technique for the Attenuation of Fin Buffet," *Journal of Aircraft*, Vol. 30, No. 6, 1993, pp. 847 – 853.

[22] Del Frate, J. H., and Zuniga, F. A., "In–Flight Flow Field Analysis on the NASA F–18 High Alpha Research Vehicle With Comparisons to Ground Facility Data," AIAA Paper 90-0231, Jan. 1990.

[23] Lee, B. H. K., "A Method for Predicting Wing Response to Buffet Loads," *Journal of Aircraft*, Vol. 21, No. 1, 1984, pp. 85-87.

[24] Lee, B. H. K., and Dunlavy, S., "Statistical Prediction of Maximum Buffet Loads on the F/A–18 Vertical Fin," *Journal of Aircraft*, Vol. 29, No. 4, 1992, pp. 734-736.

[25] Zimmermann, N. H., Ferman, M. A., Yurkovich, R. N., and Gerstenkorn, G., "Prediction of Tail Buffet Loads for Design Applications," AIAA Paper 89-1378, 1989.

[26] Lan, C. E., and Lee, I. G., "Investigation of Empennage Buffeting," NASA CR-176973, 1986.

[27] Breitsamter, C., "Messungen und Analyse der zeitabhängigen Geschwindigkeiten im wirbeldominierten Strömungsfeld

eines Hochleistungsflugzeuges, Teil 1," FLM–91/22, Lehrstuhl für Fluidmechanik, Technische Universität München, München 1991.

[28] Johnson, F. D., and Eckelmann H., "A variable angle method of calibration for X–probes applied to wall–bounded turbulent shear flow," *Experiment in Fluids* Vol. 3, No. 2, 1984, pp. 121-130.

[29] Lueptow, R. M., Breuer, K. S., and Haritonidis J. H., "Computer–aided calibration of X–probes using a look–up table," *Experiments in Fluids*, Vol. 7, No. 6, 1988, pp. 115-118.

[30] Samet, M., and Einav, S., "A hot–wire technique for simultaneous measurement of instantaneous velocities in 3D flows," *J. Phys. E: Sci. Instrum.*, Vol. 20, 1987, pp. 683-690.

[31] Cutler, A. D., and Bradshaw, P., "A Crossed Hot–Wire Technique for Complex Turbulent Flows," *Experiments in Fluids*, Vol. 12, No. 1, 1992, pp. 17 – 22.

[32] Bendat, J. S., and Piersol, A. G., "Random Data: Analysis and Measurement Procedures," J. Wiley & Sons, Inc. Ney York, 1971.

[33] Breitsamter, C., " Ein Beitrag zum Phänomen des Seitenleitwerks–Buffeting an wirbeldominierten Konfigurationen im Schiebeflug," FLM–92/41, Lehrstuhl für Fluidmechanik, Technische Universität München, München, 1992.